

# Probing the Lithium Substructure and Ionic Conductivity of the Solid Electrolyte $\text{Li}_4\text{PS}_4\text{I}$

Florian Strauss,<sup>†,\*</sup> Jing Lin,<sup>†</sup> Leonhard Karger,<sup>†</sup> Daniel Weber,<sup>†</sup> Torsten Brezesinski<sup>†</sup>

<sup>†</sup> Battery and Electrochemistry Laboratory (BELLA), Institute of Nanotechnology, Karlsruhe Institute of Technology (KIT), Hermann-von-Helmholtz-Platz 1, 76344 Eggenstein-Leopoldshafen, Germany

## Abstract

In search of high-performance solid electrolytes, various materials have been discovered in the past, approaching or even exceeding the ionic conductivity of conventional liquid electrolytes. Among the reported classes of superionic electrolytes for solid-state battery applications, lithium thiophosphates appear the most promising owing to high ionic conductivity and mechanical softness. A recent example is the  $\text{Li}_4\text{PS}_4\text{I}$  phase ( $P4/nmm$ ). Surprisingly, this material shows a comparatively low ionic conductivity at room temperature, ranging from  $10^{-4}$  to  $10^{-5}$  S  $\text{cm}^{-1}$ , despite having favorable structural characteristics. Because of discrepancies between experiment and theory regarding the Li-ion conductivity and polymorphism in  $\text{Li}_4\text{PS}_4\text{I}$ , we herein examine the crystal structure over a broad temperature range using *ex situ* and *in situ* X-ray and neutron powder diffraction techniques. We demonstrate the absence of polymorphic transitions, with a lithium redistribution at low temperatures though, and confirm the relatively poor room-temperature ionic conductivity, despite the presence of a 3D percolation network for facile charge transport.

## Introduction

Li-ion batteries (LIBs) for application in portable electronics and electric vehicles rely on the use of liquid organic electrolytes. Although conventional LIBs are approaching their physiochemical limits, higher energy and power densities would be desirable, especially for powering electric vehicles.<sup>1–3</sup> Replacing the liquid electrolyte with a solid electrolyte (SE) is considered a promising strategy to achieve improved energy and power densities over state-of-the-art LIB technologies, in addition to potentially increased safety. Various inorganic SEs based on oxides, halides, sulfides, and hydroborates have been reported in the past, showing room-temperature ionic conductivities similar to liquid electrolytes. Among them, the lithium thiophosphates possess very high ionic conductivities while having favorable mechanical properties, the latter allowing for tight contact with the active electrode material.<sup>4–9</sup> Unfortunately, these advantages come along with a poor (electro)chemical stability, which negatively affects the battery performance.<sup>10–14</sup> Although the intrinsic stability window of lithium thiophosphates is narrow, the SE/electrode material decomposition interface can be kinetically stable, thereby preventing continuous SE degradation during electrochemical cycling and allowing for stable (long-term) operation.<sup>15–19</sup>

In recent years, it has been shown that  $x\text{Li}_2\text{S}-y\text{P}_2\text{S}_5-y\text{LiI}$ -based SEs are capable of forming robust interfaces with positive and negative electrode materials in solid-state batteries.<sup>19–24</sup> An example is the recently discovered  $\text{Li}_4\text{PS}_4\text{I}$  (either as glassy  $1.5\text{Li}_2\text{S}-0.5\text{P}_2\text{S}_5-\text{LiI}$  phase or with the  $P4/nmm$  space group).<sup>25</sup> The experimental ionic conductivity of the crystalline material is surprisingly low though, in the range of  $10^{-4}$  to  $10^{-5}$   $\text{S cm}^{-1}$  at room temperature, despite the presence of 3D percolation pathways.<sup>19,25,26</sup> By contrast, density-functional theory (DFT) calculations suggest an ionic conductivity that is orders of magnitude higher than those measured.<sup>27</sup> Recent studies aiming at better understanding the discrepancy between experiment and theory showed that the crystallization of  $\text{Li}_4\text{PS}_4\text{I}$  from the glassy precursor phase leads to a strong decrease in conductivity.<sup>19,26</sup> However, the existence of a highly conductive (high-temperature) polymorph, due to phase transition at 350 K, has been predicted from *ab initio* molecular dynamics (MD) simulations.<sup>28</sup>

These apparent inconsistencies provided an impetus to re-examine the crystal structure in a broad temperature range using high-resolution *ex situ* neutron and synchrotron X-ray diffraction in combination with *in situ* laboratory X-ray diffraction. We show that the  $\text{Li}_4\text{PS}_4\text{I}$  does not undergo phase (polymorphic) transitions between 10 and 1010 K and certain crystallographic sites are important to establish a 3D percolation network for facile lithium migration.

## Experimental Section

### General

The work was conducted under argon atmosphere in a glovebox (MBraun, with  $[\text{O}_2]$  and  $[\text{H}_2\text{O}] < 0.1$  ppm), and all chemicals were used as received.

## Synthesis

Li<sub>4</sub>PS<sub>4</sub>I was prepared by mixing stoichiometric amounts of Li<sub>2</sub>S (99.9 %, Sigma Aldrich), P<sub>2</sub>S<sub>5</sub> (99 %, Sigma Aldrich), and LiI (99.999 % Sigma Aldrich) using a planetary ball mill (Fritsch). The precursors were loaded into a 250 mL zirconia milling jar and milled for 1 h at 250 rpm and subsequently for 20 h at 450 rpm, with a ball-to-powder ratio of 12:1 (10 mm diameter zirconia balls). The recovered powder was compacted into 10 mm diameter pellets at 1.5 t. The latter pellets were then sealed under vacuum (10<sup>-3</sup> mbar) in quartz ampules and annealed for 24 h at 500 °C with the heating and cooling rates set to 5 °C min<sup>-1</sup>.

## Characterization

Laboratory X-ray diffraction (XRD) measurements were conducted on samples sealed in borosilicate glass capillaries from Hilgenberg (with 0.48 mm inner diameter and 0.01 mm wall thickness) using a STADI P diffractometer (STOE) equipped with a Mo K $\alpha$ <sub>1</sub> radiation source.

Synchrotron XRD (SXR) patterns were recorded in transmission mode (with  $\lambda = 0.458199 \text{ \AA}$ ) at temperatures of  $T = 295$  and 100 K using the beamline 11-BM (Argonne National Laboratory). The samples were sealed in borosilicate glass capillaries from Hilgenberg (with 0.68 mm inner diameter and 0.01 mm wall thickness) and then inserted into the Kapton tube of the sample holder.

*In situ* high-temperature laboratory XRD measurements were performed on a customized diffractometer equipped with a microfocus rotating anode (Mo K $\alpha$ <sub>1,2</sub>), a Pilatus 300 K-W area detector, and a home-built gas flow furnace based on the design by Chupas *et al.*<sup>29,30</sup> The sample was sealed in a borosilicate glass capillary from Hilgenberg (with 0.48 mm inner diameter and 0.01 mm wall thickness) and then inserted into a sapphire capillary of diameter 1.016 mm. Temperature control was established using a thermocouple placed next to the capillary. Temperature calibration was done versus the unit-cell volume of Al<sub>2</sub>O<sub>3</sub> powder measured in a separate heating experiment.<sup>31</sup>

Neutron powder diffraction (NPD) patterns were recorded (with  $\lambda = 1.595072 \text{ \AA}$ ) at temperatures of  $T = 298$  and 10 K using the D2B high-resolution powder diffractometer (Institut Laue-Langevin). To this end, ~1.5 g of the samples were sealed in 6 mm diameter vanadium cylinders.

Rietveld analysis of diffraction data was done with the help of FullProf Suite. The Thompson-Cox-Hastings pseudo-Voigt function was used to describe the peak shape. A point-by-point background was applied. Scale factor, peak shape parameters, lattice parameters, and overall anisotropic atomic displacement parameters were refined. In the case of NPD, the atomic coordinates, individual anisotropic atomic displacement parameters, and lithium occupancies were additionally refined. The zero-shift parameter was treated last. Finally, all parameters were treated independently, further confirming the stability of the refined crystal structure. Note that for the refinement of NPD data collected at 298 K, the occupancy of the Li<sub>2</sub> and Li<sub>5</sub> sites was constraint to be 1 to avoid divergence.

Raman spectroscopy was conducted on a sample sealed in a borosilicate glass capillary from Hilgenberg (with 0.48 mm inner diameter and 0.01 mm wall thickness). The measurement was done with an excitation wavelength of  $\lambda = 532$  nm using a Renishaw in Via confocal Raman microscope.

The ionic conductivity was measured by electrochemical impedance spectroscopy (EIS) in the 100 mHz to 7.0 MHz frequency range with an AC voltage amplitude of 30 mV using an SP-300 potentiostat (Biologic). ~300 mg of the as-milled precursor mixture was compressed in a 10 mm diameter pellet die at 2 t. The pellet was then sealed under vacuum ( $10^{-3}$  mbar) in a quartz ampule and annealed for 24 h at 500 °C. Next, indium electrodes (10 mm diameter) were attached on both sides of the pellet. The EIS spectra were fitted with  $(R_1Q_1)Q_2$  equivalent circuits. The conductivity was calculated from the value of  $R_1$ , and the activation energy was determined by linear fitting of the temperature-dependent conductivity using the Arrhenius equation. Residual porosity was not taken into account.

Bond valence energy landscapes (BVELs) for lithium were calculated according to a method developed by Adams *et al.* as implemented in the program Bond\_Str of the FullProf Suite.<sup>32</sup> The software VESTA was used to generate crystal structure and BVEL images.<sup>33</sup>

## Results and Discussion

In an attempt to prepare highly crystalline  $\text{Li}_4\text{PS}_4\text{I}$ , we chose a solid-state route starting from ball-milled powder of the precursor mixture  $\text{Li}_2\text{S}$ ,  $\text{P}_2\text{S}_5$ , and  $\text{LiI}$ , with annealing carried out in a quartz ampule under vacuum at 500 °C. The laboratory XRD pattern (**Fig. S1**) showed sharp reflections pertaining to  $\text{Li}_4\text{PS}_4\text{I}$ , as well as some low-intensity reflections that can be attributed to  $\text{Li}_6\text{PS}_5\text{I}$ . To gain thorough insight into the crystal structure of  $\text{Li}_4\text{PS}_4\text{I}$ , especially the lithium substructure, high-resolution NPD data were collected both at 298 K and 10 K. The NPD patterns and corresponding Rietveld refinement plots are shown in **Fig. 1**. They can be indexed to the  $P4/nmm$  space group, in agreement with recent findings.<sup>25</sup> The  $a$  and  $c$  lattice parameters were calculated to be 8.47839(2) Å and 5.93305(4) Å at 298 K and 8.41854(2) Å and 5.88267(2) Å at 10 K, respectively, leading to unit-cell volumes of  $V = 426.486(22)$  Å<sup>3</sup> and 416.915(20) Å<sup>3</sup> (detailed structural parameters are provided in **Tabs. S1** and **S2**). The amount of argyrodite  $\text{Li}_6\text{PS}_5\text{I}$  as an impurity phase in the sample was determined to be 13-16 wt.%. Note that the formation of the argyrodite phase has been observed before in the solid-state synthesis of  $\text{Li}_4\text{PS}_4\text{I}$ .<sup>26</sup>

Complementary synchrotron XRD measurements were also conducted on the  $\text{Li}_4\text{PS}_4\text{I}$  sample at 295 K and 100 K. The experimental patterns and the lattice parameters from Rietveld refinement analysis are shown in **Fig. S2**. Overall, the *ex situ* synchrotron XRD and NPD results revealed a decrease in lattice parameters with decreasing temperature, as expected, corresponding to a unit-cell volume shrinkage by ~2.2 % from 298 K to 10 K (**Fig. S3a,b**).

*In situ* laboratory XRD patterns were collected in the temperature range 295-1010 K. A gradual shift of the  $\text{Li}_4\text{PS}_4\text{l}$  reflections to lower  $2\theta$  angles with increasing temperature was observed (**Fig. S4**), indicating an increase in unit-cell volume due to thermal expansion.

Comparing all refined lattice parameters, a linear change in  $a/b$  and  $c$  lattice parameters with temperature was noticed (**Fig. S3a**), resulting in an expansion of the unit-cell volume from  $416.915(20) \text{ \AA}^3$  at 10 K to  $457.489(2) \text{ \AA}^3$  at 1010 K (**Fig. S3b**). Considering this kind of behavior over such a broad temperature range, we assume that no phase (polymorphic) transitions occur in the material,<sup>34</sup> contrary to what has been predicted theoretically.<sup>28</sup>

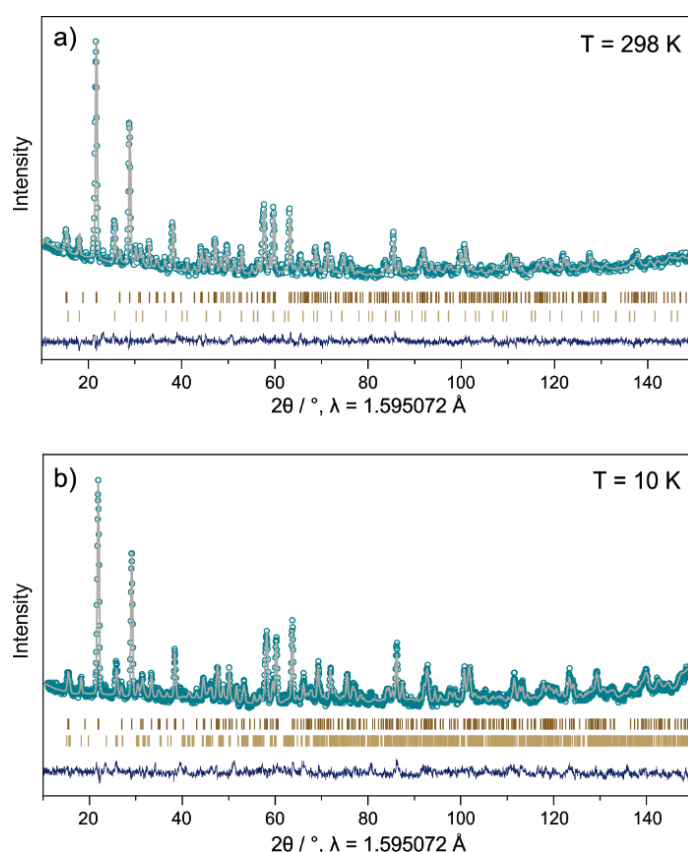


**Figure 1.** High-resolution NPD patterns of  $\text{Li}_4\text{PS}_4\text{l}$  taken at (a) 298 K and (b) 10 K and corresponding Rietveld refinement plots. Measured, calculated, and difference profiles are shown as cyan circles, gray line, and blue line, respectively. Brown and beige tick marks indicate the expected reflections for  $\text{Li}_4\text{PS}_4\text{l}$  ( $P4/nmm$  space group) and  $\text{Li}_6\text{PS}_5\text{l}$ , respectively. Note that the high-temperature ( $F-43m$  space group) or low-temperature  $\text{Li}_6\text{PS}_5\text{l}$  phase ( $C1c1$  space group) was taken into account as an impurity in the refinement analysis.<sup>35</sup>

The ambient- and low-temperature crystal structures calculated on the basis of the NPD results are shown in **Fig. 2**. For the  $\text{Li}_4\text{PS}_4\text{l}$  at 298 K, the phosphorus atoms occupy a single crystallographic site ( $2b$ ) that is tetrahedrally coordinated by sulfur ( $8i$ ), thereby forming isolated  $[\text{PS}_4]^{3-}$  units. The symmetric stretching vibrations of the

[PS<sub>4</sub>]<sup>3-</sup> tetrahedra were clearly visible as a distinct band centered at 428 cm<sup>-1</sup> in the Raman spectrum (**Fig. S5**). Less intense bands seen at 557 cm<sup>-1</sup> and 597 cm<sup>-1</sup> and below 300 cm<sup>-1</sup> originate from asymmetric bending modes of the [PS<sub>4</sub>]<sup>3-</sup> units.<sup>36</sup> The iodine atoms also occupy a single crystallographic site (2c), and the lithium atoms are distributed over five crystallographic sites (2c, 2a, 8j, 4d, and 8i) between the [PS<sub>4</sub>]<sup>3-</sup> tetrahedra and iodine atoms. Notably there are some differences to the originally reported crystal structure shown in **Fig. S6**.<sup>25</sup> This relates primarily to the lithium substructure. In particular, the Li5 site is pushed away from the [PS<sub>4</sub>]<sup>3-</sup> tetrahedra, which can also be expressed by the Li5-Li2-Li5 angle. The latter angle has been previously determined to be 122°. <sup>25</sup> However, we found it to be 171°, leading to decreasing Li4-Li5 and Li5-Li2 distances, from 2.420 Å to 2.350 Å and 1.301 Å to 1.120 Å, respectively. In contrast, the Li4-Li3 distance increased from 2.524 Å to 2.576 Å.

For the Li<sub>4</sub>PS<sub>4</sub>I at 10 K, similar [PS<sub>4</sub>]<sup>3-</sup> and iodine positions were found, with the difference being that the lithium atoms are only distributed over four instead of five crystallographic sites. This in turn leads to a distance of 2.976 Å for Li4-Li2, as Li5 as an intermediate site along this pathway is no longer available. For the Li4-Li3 distance, we found a decrease from 2.576 Å at 298 K to 2.520 Å at 10 K.

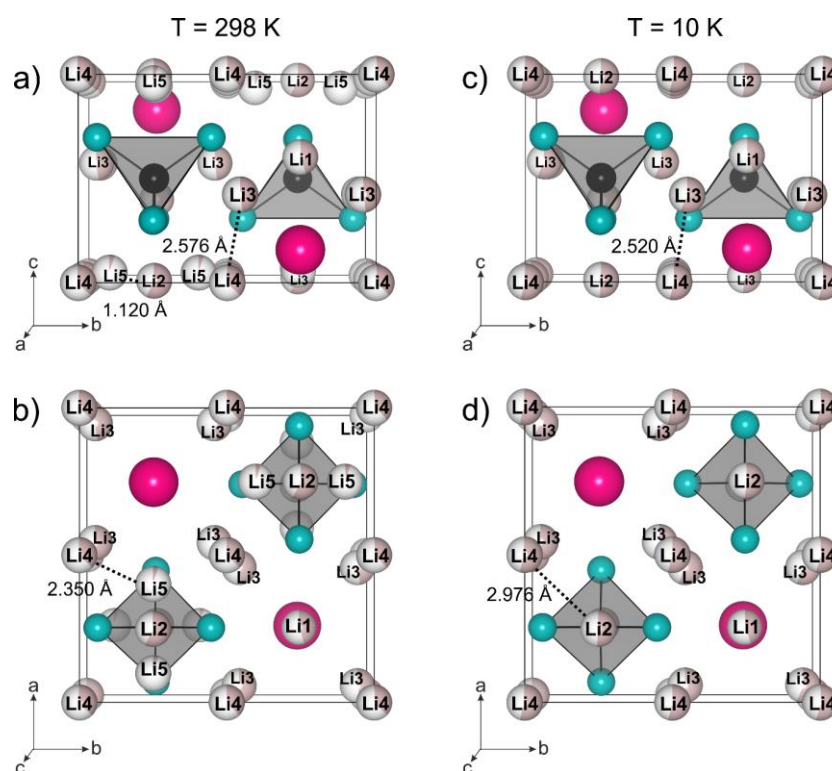


**Figure 2.** View of the crystal structure of Li<sub>4</sub>PS<sub>4</sub>I at (a,b) 298 K and (c,d) 10 K along different directions. Pink, cyan, and black spheres represent the iodine, sulfur, and phosphorus atoms. Lithium atoms occupying various crystallographic sites are shown as bronze spheres.

To gain more insight into the lithium substructure, the normalized (partial) lithium occupancies of the respective Wyckoff positions were analyzed. A graphical

representation is provided in **Fig. 3**. In the reported distribution, 30 % were placed on Li1 (2c), 26 % on Li2 (2a), 17 % on Li3 (8j), 24 % on Li4 (4d), and 3 % on Li5 (8i). Here, the normalized occupancy for Li2, Li3, and Li5 was found to be 34 %, 22 %, and 3 %, respectively. Thus, that for Li1 (28 %) and Li4 (13 %) was somewhat lower. In any case, the distribution was relatively broad at 298 K.

Upon cooling the material to 10 K, two main changes occurred in the lithium substructure. First, the Li5 site was unoccupied, in agreement with recent DFT calculations, showing that Li5 possesses the highest site energy (the calculated site energy for lithium apparently increases in the order:  $\text{Li1} < \text{Li3} < \text{Li2} < \text{Li4} < \text{Li5}$ ).<sup>28</sup> This result suggests that Li5 can be considered a kind of “smeared out” lithium density of Li2. Note that thermal displacement is minor at very low temperatures. Second, the lithium distribution over the remaining sites converged, ranging from 21 % to 28 %. Overall, the sum of freely refined lithium occupancies results in a stoichiometry of  $\text{Li}_{4.2}\text{PS}_4\text{I}$  at 298 K and  $\text{Li}_{4.0}\text{PS}_4\text{I}$  at 10 K, lying within the standard deviation range and being in good agreement with the targeted composition.

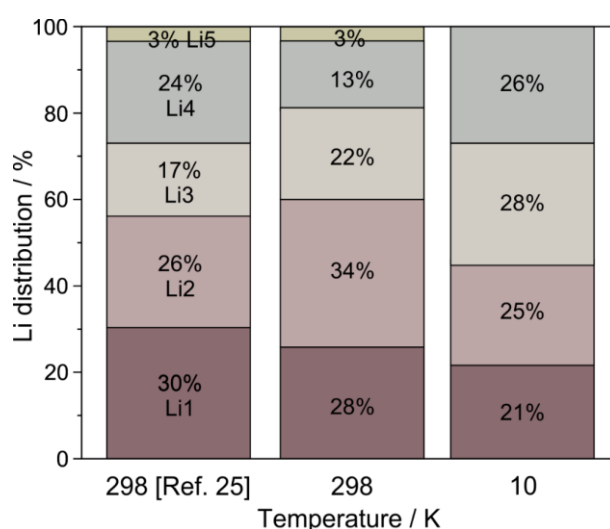


**Figure 3.** Normalized lithium distribution over the different crystallographic sites as reported in literature and determined by NPD in this work.

Finally, the BVEL approach was utilized to visualize the differences in lithium diffusion pathways. **Fig. 4** shows the calculated BVELs with an energy of  $E_{\text{BVSE}}(\text{Li}) = 1.6$  eV over the global minimum. For the room-temperature structure, we found that, except for Li1, all lithium atoms are involved in forming a 3D percolation network, in contrast to what has been suggested in literature.<sup>25,27</sup> This is probably a result of the high migration barrier for Li1, which is reflected in the large distance to the next-neighboring lithium site (Li3).<sup>28</sup> For the  $\text{Li}_4\text{PS}_4\text{I}$  at 10 K, only Li3 and Li4 are involved in the lithium migration pathways, leading to anisotropic transport along the *c*-axis, with Li1 and Li2 most likely not contributing to long-range ion transport, as they are isolated towards the other lithium sites (large Li-Li distances). We conclude from the data that partial filling of the Li5 site is required to facilitate lithium diffusion in  $\text{Li}_4\text{PS}_4\text{I}$ . In particular, Li5 constitutes an intermediate site situated along the Li4-Li2 pathway (connecting the Li4 and Li2 sites), thus decreasing the activation energy for ion hopping and improving

(3D) lithium percolation throughout the structure. This is also consistent with the assumption of “smeared out” lithium density resulting from the fast exchange between the two neighboring sites at elevated temperatures.

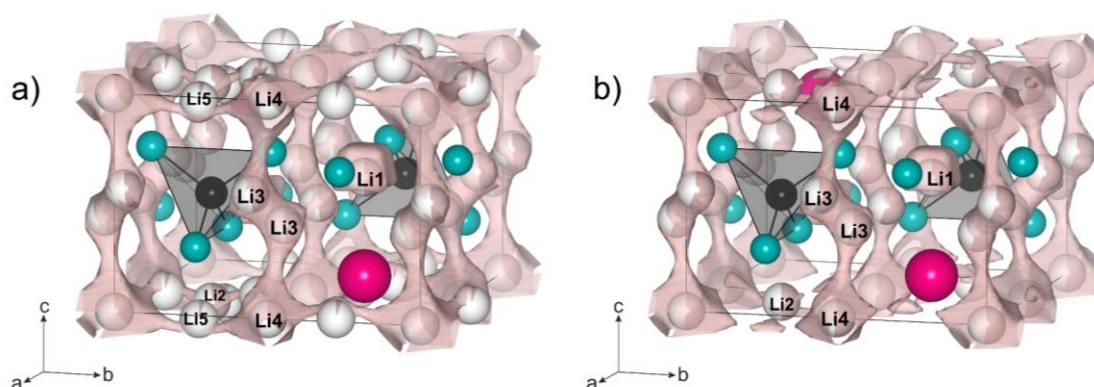


**Figure 4.** Bond valence energy landscapes for  $\text{Li}_4\text{PS}_4\text{I}$  at (a) 298 K and (b) 10 K showing the lithium conduction pathways (bronze trajectories). Pink, cyan, and black spheres represent the iodine, sulfur, and phosphorus atoms. Lithium atoms occupying various crystallographic sites are shown as bronze spheres.

Lastly, EIS measurements were conducted on a sintered pellet in the temperature range 298-338 K. A representative Nyquist plot of the electrochemical impedance of  $\text{Li}_4\text{PS}_4\text{I}$  at 298 K is shown in **Fig. S7**. The spectra revealed a semicircle and a capacitive tail. They were fitted assuming an  $(R_1Q_1)Q_2$  equivalent circuit. For the semicircle, a capacitance of  $1.1 \cdot 10^{-10}$  F was determined. We note that the capacitance is about one to two orders of magnitude larger than that usually found for the bulk conductivity of dense Li-ion conductors,<sup>37-39</sup> probably partly because of the presence of  $\text{Li}_6\text{PS}_5\text{I}$  as an impurity phase (and the related grain boundary conductivity contribution). **Fig. 5** shows the temperature-dependent conductivity determined from the  $R_{\text{bulk}}$ , indicating Arrhenius-type behavior. The activation energy for conduction and room-temperature ionic conductivity were calculated to be 0.45 eV and  $0.022 \text{ mS cm}^{-1}$ , respectively. The conductivity is clearly affected to some (unknown) degree by the aforementioned argyrodite phase, which itself has been reported to have an ionic conductivity in the region of  $10^{-6} \text{ S cm}^{-1}$  at room temperature (with a similar activation energy for conduction to that of  $\text{Li}_4\text{PS}_4\text{I}$ ).<sup>38,40</sup> Nevertheless, both values agree with data available in literature and confirm the intrinsic limitations of the crystalline  $\text{Li}_4\text{PS}_4\text{I}$  (despite having favorable structural characteristics).<sup>19,25,26</sup>

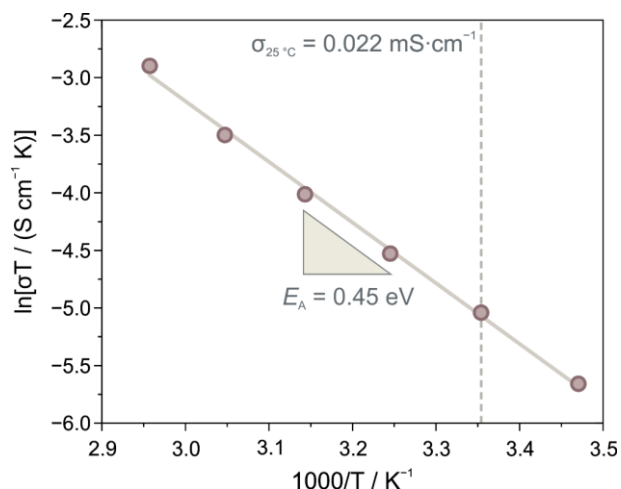


**Figure 5.** Arrhenius plot of the conductivity of Li<sub>4</sub>PS<sub>4</sub>I in the temperature range from 298 K to 338 K.

## Conclusion

In summary, we have probed the crystal structure of the solid electrolyte Li<sub>4</sub>PS<sub>4</sub>I in a broad temperature range by *ex situ* and *in situ* X-ray and neutron powder diffraction. The occurrence of polymorphic transitions in Li<sub>4</sub>PS<sub>4</sub>I can be ruled out. However, changes in lithium occupancy are observed at low temperatures ( $T = 10$  K). Although Li<sub>4</sub>PS<sub>4</sub>I offers a 3D percolation network for facile lithium migration, the room-temperature conductivity ( $\sim 0.02$  mS cm<sup>-1</sup>) is confirmed to be relatively low, especially compared to argyrodite lithium thiophosphate electrolytes. Despite the presence of a substantial amount of Li<sub>6</sub>PS<sub>5</sub>I as an impurity phase, we assume that the poor conductivity is intrinsic in nature. Yet, the Li<sub>4</sub>PS<sub>4</sub>I structure may be a good starting point for improvements in ionic conductivity via aliovalent/isovalent doping or substitution.

## Associated Content

### Supporting information

The Supporting Information is available free of charge on the ACS Publications website at DOI: Laboratory and synchrotron XRD patterns; temperature-dependent lattice parameters and unit-cell volume; *in situ* high-temperature XRD data; Raman spectroscopy data; representative Nyquist plot of the electrochemical impedance; structural parameters from Rietveld refinement analysis.

## Author Information

### Corresponding Author

\*Phone: +49 721 608 26536; Email: [florian.strauss@kit.edu](mailto:florian.strauss@kit.edu)

## Notes

The authors declare no competing financial interest.

## Acknowledgements

F.S. acknowledges the Fonds der Chemischen Industrie (FCI) for financial support through a Liebig fellowship. J.L. is grateful to FCI for PhD funding. This work was partially supported by BASF SE. The authors thank Dr. Clemens Ritter for collecting the neutron diffraction data and Institut Laue-Langevin (ILL) for beamtime allocation under proposal number (5-21-1164), DOI:10.5291/ILL-DATA.5-21-1164. Use of the Advanced Photon Source at Argonne National Laboratory was supported by the U. S. Department of Energy, Office of Science, Office of Basic Energy Sciences, under contract no. DE-AC02-06CH11357. The authors thank Dr. Holger Geßwein for providing assistance with the *in situ* high-temperature XRD measurements.

## References

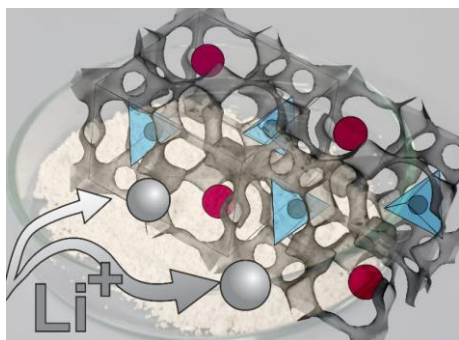
- (1) Janek, J.; Zeier, W. G. A Solid Future for Battery Development. *Nat. Energy* **2016**, *1*, 16141.
- (2) Kato, Y.; Hori, S.; Saito, T.; Suzuki, K.; Hirayama, M.; Mitsui, A.; Yonemura, M.; Iba, H.; Kanno, R. High-Power All-Solid-State Batteries Using Sulfide Superionic Conductors. *Nat. Energy* **2016**, *1*, 16030.
- (3) Lee, Y.-G.; Fujiki, S.; Jung, C.; Suzuki, N.; Yashiro, N.; Omoda, R.; Ko, D.-S.; Shiratsuchi, T.; Sugimoto, T.; Ryu, S.; Ku, J. H.; Watanabe, T.; Park, Y.; Aihara, Y.; Im, D.; Han, I. T. High-Energy Long-Cycling All-Solid-State Lithium Metal Batteries Enabled by Silver–carbon Composite Anodes. *Nat. Energy* **2020**, *5*, 299–308.
- (4) Reddy, M. V.; Julien, C. M.; Mauger, A.; Zaghbi, K. Sulfide and Oxide Inorganic Solid Electrolytes for All-Solid-State Li Batteries: A Review. *Nanomaterials* **2020**, *10*, 1606.
- (5) Lau, J.; DeBlock, R. H.; Butts, D. M.; Ashby, D. S.; Choi, C. S.; Dunn, B. S. Sulfide Solid Electrolytes for Lithium Battery Applications. *Adv. Energy Mater.* **2018**, *8*, 1800933.
- (6) Lee, H.; Oh, P.; Kim, J.; Cha, H.; Chae, S.; Lee, S.; Cho, J. Advances and Prospects of Sulfide All-Solid-State Lithium Batteries via One-to-One Comparison with Conventional Liquid Lithium Ion Batteries. *Adv. Mater.* **2019**, *31*, 1900376.
- (7) Koerver, R.; Zhang, W.; de Biasi, L.; Schweidler, S.; Kondrakov, A. O.; Kolling, S.; Brezesinski, T.; Hartmann, P.; Zeier, W. G.; Janek, J. Chemo-Mechanical Expansion of Lithium Electrode Materials – On the Route to Mechanically Optimized All-Solid-State Batteries. *Energy Environ. Sci.* **2018**, *11*, 2142–2158.

- (8) McGrogan, F. P.; Swamy, T.; Bishop, S. R.; Eggleton, E.; Porz, L.; Chen, X.; Chiang, Y.-M.; Vliet, K. J. V. Compliant Yet Brittle Mechanical Behavior of  $\text{Li}_2\text{S}-\text{P}_2\text{S}_5$  Lithium-Ion-Conducting Solid Electrolyte. *Adv. Energy Mater.* **2017**, *7*, 1602011.
- (9) Tippens, J.; Miers, J. C.; Afshar, A.; Lewis, J. A.; Cortes, F. J. Q.; Qiao, H.; Marchese, T. S.; Di Leo, C. V.; Saldana, C.; McDowell, M. T. Visualizing Chemomechanical Degradation of a Solid-State Battery Electrolyte. *ACS Energy Lett.* **2019**, *4*, 1475–1483.
- (10) Xiao, Y.; Wang, Y.; Bo, S.-H.; Kim, J. C.; Miara, L. J.; Ceder, G. Understanding Interface Stability in Solid-State Batteries. *Nat. Rev. Mater.* **2019**, *5*, 105–126.
- (11) Auvergniot, J.; Cassel, A.; Ledeuil, J.-B.; Viallet, V.; Seznec, V.; Dedryvère, R. Interface Stability of Argyrodite  $\text{Li}_6\text{PS}_5\text{Cl}$  toward  $\text{LiCoO}_2$ ,  $\text{LiNi}_{1/3}\text{Co}_{1/3}\text{Mn}_{1/3}\text{O}_2$ , and  $\text{LiMn}_2\text{O}_4$  in Bulk All-Solid-State Batteries. *Chem. Mater.* **2017**, *29*, 3883–3890.
- (12) Richards, W. D.; Miara, L. J.; Wang, Y.; Kim, J. C.; Ceder, G. Interface Stability in Solid-State Batteries. *Chem. Mater.* **2016**, *28*, 266–273.
- (13) Koerver, R.; Aygün, I.; Leichtweiß, T.; Dietrich, C.; Zhang, W.; Binder, J. O.; Hartmann, P.; Zeier, W. G.; Janek, J. Capacity Fade in Solid-State Batteries: Interphase Formation and Chemomechanical Processes in Nickel-Rich Layered Oxide Cathodes and Lithium Thiophosphate Solid Electrolytes. *Chem. Mater.* **2017**, *29*, 5574–5582.
- (14) Strauss, F.; Kitsche, D.; Ma, Y.; Teo, J. H.; Goonetilleke, D.; Janek, J.; Bianchini, M.; Brezesinski, T. Operando Characterization Techniques for All-Solid-State Lithium-Ion Batteries. *Adv. Energy Sustain. Res.* **2021**, *2*, 2100004.
- (15) Haruyama, J.; Sodeyama, K.; Han, L.; Takada, K.; Tateyama, Y. Space-charge Layer Effect at Interface between Oxide Cathode and Sulfide Electrolyte in All-Solid-State Lithium-Ion Battery. *Chem. Mater.* **2014**, *26*, 4248–4255.
- (16) Zhu, Y.; He, X.; Mo, Y. Origin of Outstanding Stability in the Lithium Solid Electrolyte Materials: Insights from Thermodynamic Analyses Based on First-Principles Calculations. *ACS Appl. Mater. Interfaces* **2015**, *7*, 23685–23693.
- (17) Xu, L.; Tang, S.; Cheng, Y.; Wang, K.; Liang, J.; Liu, C.; Cao, Y.-C.; Wei, F.; Mai, L. Interfaces in Solid-State Lithium Batteries. *Joule* **2018**, *2*, 1991–2015.
- (18) Nakamura, T.; Amezawa, K.; Kulisch, J.; Zeier, W. G.; Janek, J. Guidelines for All-Solid-State Battery Design and Electrode Buffer Layers Based on Chemical Potential Profile Calculation. *ACS Appl. Mater. Interfaces* **2019**, *11*, 19968–19976.
- (19) Strauss, F.; Teo, J. H.; Janek, J.; Brezesinski, T. Investigations into the Superionic Glass Phase of  $\text{Li}_4\text{PS}_4\text{l}$  for Improving the Stability of High-Loading All-Solid-State Batteries. *Inorg. Chem. Front.* **2020**, *7*, 3953–3960.

- (20) Bron, P.; Roling, B.; Dehnen, S. Impedance Characterization Reveals Mixed Conducting Interphases between Sulfidic Superionic Conductors and Lithium Metal Electrodes. *J. Power Sources* **2017**, *352*, 127–134.
- (21) Han, F.; Yue, J.; Zhu, X.; Wang, C. Suppressing Li Dendrite Formation in Li<sub>2</sub>S–P<sub>2</sub>S<sub>5</sub> Solid Electrolyte by Lil Incorporation. *Adv. Energy Mater.* **2018**, *8*, 1703644.
- (22) Singh, N.; Horwath, J. P.; Bonnicksen, P.; Suto, K.; Stach, E. A.; Matsunaga, T.; Muldoon, J.; Arthur, T. S. Role of Lithium Iodide Addition to Lithium Thiophosphate: Implications beyond Conductivity. *Chem. Mater.* **2020**, *32*, 7150–7158.
- (23) Kato, A.; Yamamoto, M.; Sakuda, A.; Hayashi, A.; Tatsumisago, M. Mechanical Properties of Li<sub>2</sub>S–P<sub>2</sub>S<sub>5</sub> Glasses with Lithium Halides and Application in All-Solid-State Batteries. *ACS Appl. Energy Mater.* **2018**, *1*, 1002–1007.
- (24) Teo, J. H.; Strauss, F.; Walther, F.; Ma, Y.; Payandeh, S.; Scherer, T.; Bianchini, M.; Janek, J.; Brezesinski, T. The Interplay between (Electro)chemical and (Chemo)mechanical Effects in the Cycling Performance of Thiophosphate-Based Solid-State Batteries. *Mater. Futures* **2022**, *1*, 015102.
- (25) Sedlmaier, S. J.; Indris, S.; Dietrich, C.; Yavuz, M.; Dräger, C.; von Seggern, F.; Sommer, H.; Janek, J. Li<sub>4</sub>PS<sub>4</sub>I: A Li<sup>+</sup> Superionic Conductor Synthesized by a Solvent-Based Soft Chemistry Approach. *Chem. Mater.* **2017**, *29*, 1830–1835.
- (26) Strauss, F.; Lin, J.; Janek, J.; Brezesinski, T. Influence of Synthesis Parameters on Crystallization Behavior and Ionic Conductivity of the Li<sub>4</sub>PS<sub>4</sub>I Solid Electrolyte. *Sci. Rep.* **2021**, *11*, 14073.
- (27) Siculo, S.; Kalcher, C.; Sedlmaier, S. J.; Janek, J.; Albe, K. Diffusion Mechanism in the Superionic Conductor Li<sub>4</sub>PS<sub>4</sub>I Studied by First-Principles Calculations. *Solid State Ion.* **2018**, *319*, 83–91.
- (28) Prasada Rao, R.; Chen, H.; Adams, S. Stable Lithium Ion Conducting Thiophosphate Solid Electrolytes Li<sub>x</sub>(PS<sub>4</sub>)<sub>y</sub>X<sub>z</sub> (X = Cl, Br, I). *Chem. Mater.* **2019**, *31*, 8649–8662.
- (29) Biasi, L. de; Lieser, G.; Rana, J.; Indris, S.; Dräger, C.; Glatthaar, S.; Mönig, R.; Ehrenberg, H.; Schumacher, G.; Binder, J. R.; Geßwein, H. Unravelling the Mechanism of Lithium Insertion into and Extraction from Trirutile-Type LiNiFeF<sub>6</sub> Cathode Material for Li-Ion Batteries. *CrystEngComm* **2015**, *17*, 6163–6174.
- (30) Chupas, P. J.; Chapman, K. W.; Kurtz, C.; Hanson, J. C.; Lee, P. L.; Grey, C. P. A Versatile Sample-Environment Cell for Non-Ambient X-Ray Scattering Experiments. *J. Appl. Crystallogr.* **2008**, *41*, 822–824.
- (31) Stinton, G. W.; Evans, J. S. O. Parametric Rietveld Refinement. *J. Appl. Crystallogr.* **2007**, *40*, 87–95.
- (32) Adams, S. From Bond Valence Maps to Energy Landscapes for Mobile Ions in Ion-Conducting Solids. *Solid State Ion.* **2006**, *177*, 1625–1630.

- (33) Momma, K.; Izumi, F. VESTA 3 for Three-Dimensional Visualization of Crystal, Volumetric and Morphology Data. *J. Appl. Cryst.* **2011**, *44*, 1272–1276.
- (34) Salje, E. K. H. Crystallography and Structural Phase Transitions, an Introduction. *Acta Crystallogr. A* **1991**, *47*, 453–469.
- (35) Kong, S.-T.; Deiseroth, H.-J.; Reiner, C.; Gün, Ö.; Neumann, E.; Ritter, C.; Zahn, D. Lithium Argyrodites with Phosphorus and Arsenic: Order and Disorder of Lithium Atoms, Crystal Chemistry, and Phase Transitions. *Chem. Eur. J.* **2010**, *16*, 2198–2206.
- (36) Pätzmann, U.; Brockner, W. Schwingungsspektren von  $\text{Ag}_3\text{PS}_4$  und  $\text{Cu}_3\text{PS}_4$  / Vibrational Spectra of  $\text{Ag}_3\text{PS}_4$  and  $\text{Cu}_3\text{PS}_4$ . *Z. Naturforschung A* **1983**, *38*, 27–30.
- (37) Irvine, J. T. S.; Sinclair, D. C.; West, A. R. Electroceramics: Characterization by Impedance Spectroscopy. *Adv. Mater.* **1990**, *2*, 132–138.
- (38) Hanghofer, I.; Brinek, M.; Eisbacher, S. L.; Bitschnau, B.; Volck, M.; Hennige, V.; Hanzu, I.; Rettenwander, D.; Wilkening, H. M. R. Substitutional Disorder: Structure and Ion Dynamics of the Argyrodites  $\text{Li}_6\text{PS}_5\text{Cl}$ ,  $\text{Li}_6\text{PS}_5\text{Br}$  and  $\text{Li}_6\text{PS}_5\text{I}$ . *Phys. Chem. Chem. Phys.* **2019**, *21*, 8489–8507.
- (39) Strauss, F.; Zinkevich, T.; Indris, S.; Brezesinski, T.  $\text{Li}_7\text{GeS}_5\text{Br}$ —An Argyrodite Li-Ion Conductor Prepared by Mechanochemical Synthesis. *Inorg. Chem.* **2020**, *59*, 12954–12959.
- (40) Kraft, M. A.; Culver, S. P.; Calderon, M.; Böcher, F.; Krauskopf, T.; Senyshyn, A.; Dietrich, C.; Zevalkink, A.; Janek, J.; Zeier, W. G. Influence of Lattice Polarizability on the Ionic Conductivity in the Lithium Superionic Argyrodites  $\text{Li}_6\text{PS}_5\text{X}$  (X = Cl, Br, I). *J. Am. Chem. Soc.* **2017**, *139*, 10909–10918.

## TOC Graphic



The Li<sub>4</sub>PS<sub>4</sub>I solid electrolyte provides a 3D Li percolation network that potentially allows for facile ion transport.